Rochester Institute of Technology

RIT Digital Institutional Repository

6-1-2005

Performance Comparison of Hyperspectral Target Detection Algorithms in Altitude Varying Scenes

Adam P. Cisz
Rochester Institute of Technology

John Schott
Rochester Institute of Technology

Follow this and additional works at: https://repository.rit.edu/article

Recommended Citation

Performance Comparison of Hyperspectral Target Detection Algorithms in Altitude Varying Scenes

Adam P. Cisz and John R. Schott

Digital Imaging and Remote Sensing Laboratory, Rochester Institute of Technology,
Rochester, NY USA

ABSTRACT

Many different hyperspectral target detection algorithms have been developed and tested under various assumptions, methods, and data sets. This work examines the spectral angle mapper (SAM), adaptive coherence estimator (ACE), and constrained energy maximization (CEM) algorithms. Algorithm performance is examined over multiple images, targets, and backgrounds. Methods to examine algorithm performance are plentiful and several different metrics are used here. Quantitative metrics are used to make direct comparisons between algorithms. Further analysis using visual performance metrics is made to examine interesting trends in the data. Results show an increase in detection algorithm performance as image altitude increases and spatial information decreases. Theories to explain this phenomenon are introduced.

Keywords: target detection, matched filters, hyperspectral imagery, performance metrics

1. INTRODUCTION

Hyperspectral target detection algorithms are used to locate predefined targets in a hyperspectral data set. Many different algorithms have been developed to accomplish this task based on numerous theories and assumptions. Most of these algorithms were developed and initially tested using a specific data set (sensor, location, target, and background description). Many of them have undergone further testing on other data sets. Throughout this process the theory and procedures for each algorithm have been well described and tested. This work implements three of these algorithms over a range of data consisting of multiple spatial resolutions. Increasing the size of the data set allows for a more robust performance evaluation of the detectors to be made. Data taken at three altitudes is examined for multiple targets in multiple backgrounds over a collection of target detection algorithms. Algorithm performance evaluation represents the other focus of this work. Current techniques to evaluate the performance of detection algorithms contain inherent difficulties when dealing with real data. New methods to compare outputs are continuously being developed and presented. Several such summary metrics are presented here and used in the overall evaluation.

2. DETECTION MODELS AND ALGORITHMS

Hyperspectral target detection is the process of locating pixels in a hyperspectral data set that correspond to a predetermined target spectrum. Each pixel in a data set consists of the measured radiance collected from all materials within that pixels instantaneous field of view (IFOV). These radiance values are subject to atmospheric and sensor effects. In many detection experiments, including this one, useful ground truth or library reflectance data may exist. Two approaches for converting data into the same space are the creation of an invariant target subspace and atmospheric compensation. The creation of an invariant target subspace converts a reflectance target vector into a subspace of radiance target vectors that span the possible variations from atmospheric and illumination effects.[1] The approach used here is an atmospheric compensation model called the Empirical Line Model (ELM). The ELM converts radiance values to reflectance values using *a priori* information about the scene.

The reflectance spectrum of every material can be used to characterize that material. The exact spectral signature of a material is highly variable however. This variability is present in remotely sensed data as well as experimental and labratory measurements of materials. Multiple ground truth measurements are often combined

---

Email: apc2125@cis.rit.edu

to better identify the spectral nature of a material. This variability can be due to surface variations, sensor noise, and illumination conditions. The spectral signature variability increases dramatically in airborn remotely sensed data. Atmospheric effects, mixed pixels, illumination, and location all further alter the spectral appearance of a material.[2]

There are two main approaches to describing the spectral variability in a scene. Structured, or geometrical, modeling assumes that the spectrum of any pixel is made up of a combination of endmember pixels that span the complexity of the image space. Unstructured, or statistical, modeling attempts to describe the spectral variation in terms of probability distributions. In general, these distributions are described using the mean vector and covariance matrix of the data assuming a multivariate normal gaussian distribution.

2.1. Target Detection in Structured (Geometrical) Models

The target detection problem when using structured models to describe the variability in a pixel is summarized in the hypothesis test

$$
\begin{aligned}
H_0 &: x = Bb + \epsilon \\
H_1 &: x = sa + Bb + \epsilon
\end{aligned}
\tag{1}
$$

where $\mathbf{B}$ is a matrix of background vectors, $\mathbf{s}$ is a target vector, and $\mathbf{a}$ and $\mathbf{b}$ are weighting vectors. The vector ϵ represents unknown errors due to noise and modeling error. The background vectors can be calculated from a number of different methods. Endmember selection methods (such as PPI and MaxD) extract vectors representing real pixels in the scene. Methods that do not result in real pixel vectors (such as SVD) generate basis vectors that can also be linearly combined to create the background space.

Target detection methods using structured background models include the adaptive subspace detector (ASD) and the orthogonal subspace projector (OSP). These and other structured algorithms have been extensively studied and published on.[2,3] This work will include one algorithm that could be classified in this category but does not use background vectors.

The spectral angle mapper (SAM) can be considered a baseline detection algorithm. SAM is calculated as the angle between a target vector and a pixel

$$
T_{SAM}(x) = cos^{-1} \frac{s^T x}{(s^T s)^{1/2} (x^T x)^{1/2}}
\tag{2}
$$

with smaller angles corresponding to a closer match between the pixels. This work does not focus on structured models but can easily be extended to include results from target detection in structured models other than SAM.

2.2. Target Detection in Unstructured (Statistical) Models

If statistical models are used to describe the variability in a pixel, then the competing hypotheses are

$$
\begin{aligned}
H_0 &: x = \beta \\
H_1 &: x = sa + \beta
\end{aligned}
\tag{3}
$$

where β corresponds to the background modeled as a multivariate normal distribution with zero mean and covariance matrix Σ ($\beta \sim N(0,\Sigma)$). For this work, the covariance matrix is obtained from the image and is assumed to follow the assumptions stated above.

There exists a series of statistical matched filter algorithms that have been derived from the generalized likelihood ratio test (GLRT) which is expressed as:

$$
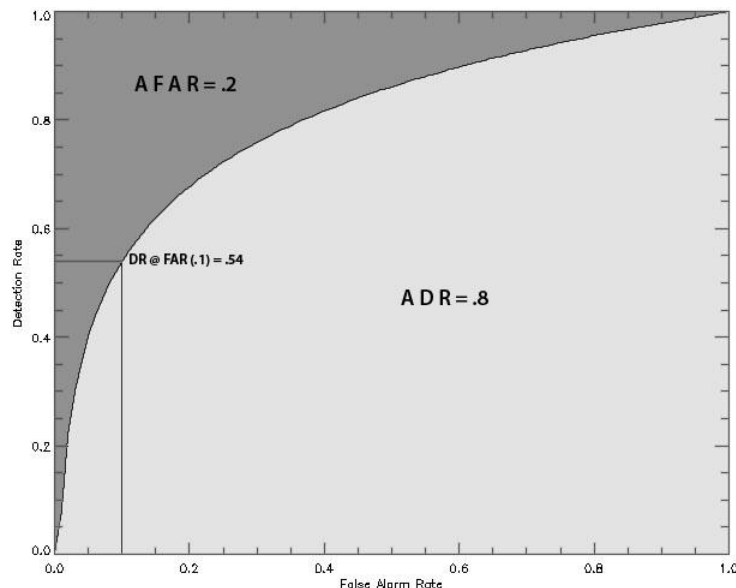T_{GLRT}(x) = \frac{(s^T \Sigma^{-1} x)^2}{(s^T \Sigma^{-1} s)(1 + x^T \Sigma^{-1} x)}.
\tag{4}
$$

Figure 1. Illustration of DR @ FAR, AFAR, and ADR comparison metrics calculated from ROC curves

This paper utilizes an algorithm that is derived from the GLRT. The adaptive coherence estimator (ACE) algorithm has been derived and exhibited success in other works.[3–5] Its association with the GLRT algorithm as it is written as

$$T_{ACE}(x) = \frac{(s^T\Sigma^{-1}x)^2}{(s^T\Sigma^{-1}s)(x^T\Sigma^{-1}x)}. \tag{5}$$

The third and final algorithm examined here is the constrained energy maximization (CEM) detector.[6] This algorithm was developed with the idea to surpress the unwanted background data while enhancing the target information in a pixel. Similarities to the GLRT and ACE algorithms can also be seen in the CEM algorithm

$$T_{CEM}(x) = \frac{s^T\Sigma^{-1}x}{s^T\Sigma^{-1}s}. \tag{6}$$

3. COMPARISON METRICS

Practical performance evaluation of target detection algorithms is quite difficult due to the inherent nature of the problem. Target detection often involves the search for a small number of target pixels in a large scene. Traditional metrics such as reciever operator characteristic (ROC) curves are not ideally suited for this problem but can be used for larger targets. ROC curves are a plot of the false alarm rate (FAR) versus the detection rate (DR) for a given target. In situations where accurate ROC curves can be generated, metrics can be extracted from these curves for comparison purposes. One such metric that can be extracted from ROC curves is the DR at a specific FAR. Other metrics that can be obtained from ROC curves are the average false alarm rate (AFAR) and the average detection rate (ADR).[7] These three metrics are illustrated in Figure 1. The AFAR metric is calculated as the area above the ROC curve and the ADR metric is area under the ROC curve. These metrics are complimentary and therefore one or the other should be used. For practical purposes, the AFAR can be calculated by averaging the FAR at each DR for a specific number of target pixels as in

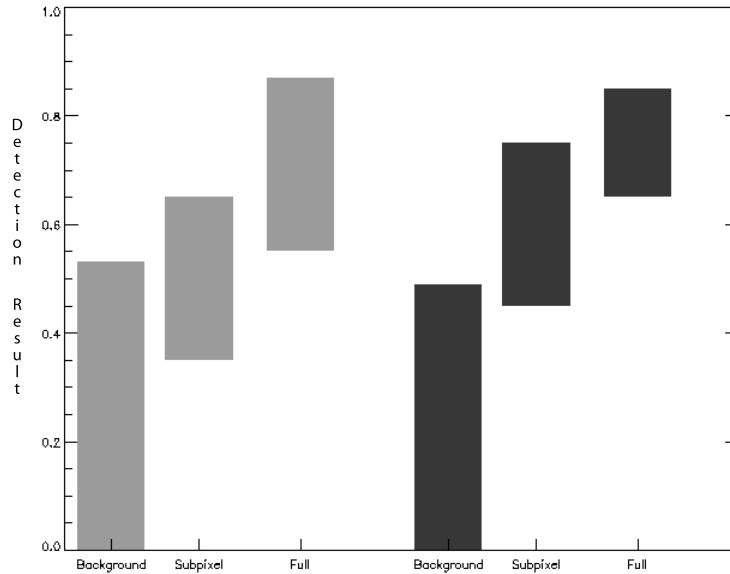$$AFAR = \frac{1}{N}\sum_{i=1}^{n} FAR_i. \tag{7}$$

Figure 2. Illustration of visual metric displaying range of values for background and targets.

where **N** represents the number of targets and **FAR** is the false alarm rate at each target **i**. The ADR is then calculated as the compliment of this value. Partial values can also be calculated for the AFAR and the ADR by limiting the number of target pixels examined and setting a maximum FAR respectively. These metrics all capture more information about the overall shape of the ROC curve than calculating a DR at a specific FAR. AFAR and ADR are also independent of any user specified limitation that can be adjusted to influence results. These metrics should only be used to make relative comparisons about common data sets.

Limitations in the number of target pixels in a scene can make the development of accurate ROC curves difficult. Experiments with a small target set are ill suited for computing ROC curves and the subsequent metrics associated with them. As a result, several different visual comparison metrics have been used to make this comparison. These visual comparison metrics seek to better illustrate the detection results than a simple display of raw results can. Displaying raw detection results does not allow one to compare metrics in an unbiased fashion due to pre-existing knowledge of the target locations. The detection values themselves should be analyzed rather than scaled maps of the results. This eliminates the use of any spatial information when analyzing results.

One such metric is used here to illustrate the target visibility enhancement in detection algorithms.[3] This visual displays the range of detection values for target pixels as well as the background. This metric has so far been limited to the use of comparing full targets to background pixels but can easily be extended to also include the relationship to subpixel targets. The bar charts in Figure 2 illustrate how this visual metric can be used to distinguish the ranges of values for background, sub, and full pixels.

Another visual metric that has been used to display the differences between full and subpixel targets and background pixels utilizes a histogram in its comparison. In this metric, background pixels are plotted as a histogram while target pixels are plotted as delta functions as seen in Figure 3.[4] The height of the delta function corresponds to the type of target pixel (full, subpixel, shadow, etc). Plotting the background pixels as a histogram allows for a better visualization of the separation between background and target.

This work attempts to illustrate the similarities and differences between these metrics as it relates to realistic data. When possible, a combination of these metrics is used. However, when large combinations of images, targets, and algorithms are used, the amount of results becomes unmanageable. The use of visual metrics is ill suited for comparing large amounts of data. In these circumstances, single value metrics are used to make the overall comparison. Visual metrics are used to better illustrate differences when varying one of the image, target, background, or algorithm parameters.
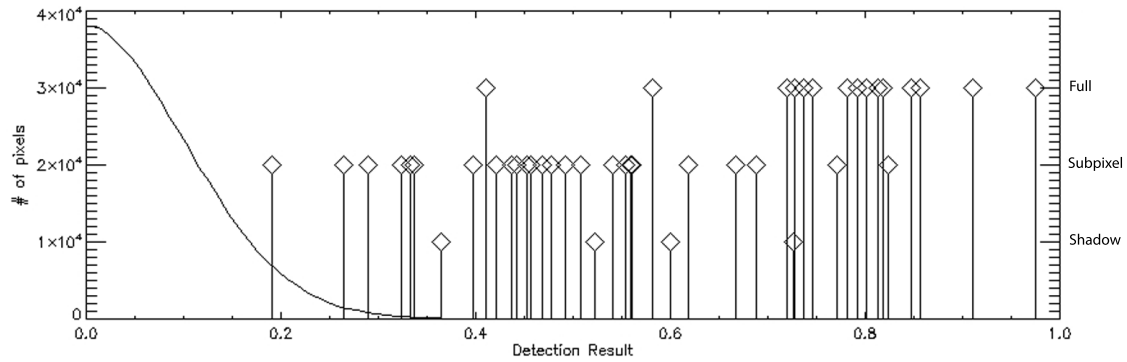
Figure 3. Illustration of visual metric displaying background as a histogram and targets as delta functions. Height of delta function indicates type of target.
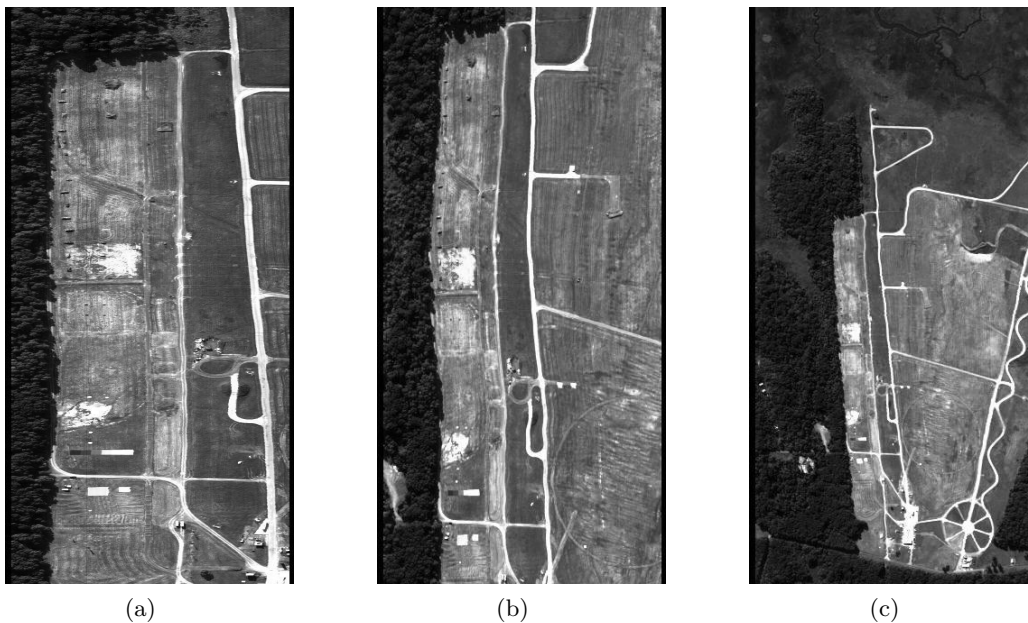

Figure 4. Greyscale images of data sets at increasing altitudes (a) Run 5 @ 5000ft, (b) Run 7 @ 10000ft, and (c) Run 9 @ 20000ft

4. DATA SET

The data used for this experiment comes from the Forest Radiance I data set collected with the HYDICE sensor. Three radiance images have been selected from this data set taken at increasing altitudes on the same day. The three runs chosen are shown in Figure 4 at altitudes of 5000, 10000, and 20000 feet. The sensor collected data in 210 spectral bands ranging from 350-2500 nm. The spectral data was then reduced by eliminating bands located in or around atmospheric absorption features.

Each of these images was converted from radiance to reflectance data by atmospherically compensating using the ELM. The decision to use atmospherically compensated data instead of radiance data was made to allow for the use of ground truth data collected for the Forest Radiance I data set. Ground truth reflectance measurements of six calibration panels allowed for a good conversion to reflectance data using ELM.

Numerous target panels and man-made objects are also present in the scene and ground truth reflectance measurements exist for these as well. Four targets were chosen for this experiment based on their size and difficulty to detect. All four of the targets are present in more than one location in each image. Two of the

Figure 5. Grass, Tree, and Road sections from Run 5 for background covariance calculation

Altitude (ft)	SAM	ACE			CEM		
		Grass	Tree	Road	Grass	Tree	Road
5000	X	X	X	X	X	X	X
10000	X	X	X	X	X	X	X
20000	X	X	X	O	X	X	O

Table 1. Summary of calculations performed

chosen targets occupy multiple full pixels in every image. The other two targets occur in three or more locations, each one having the same shape at different orientations.

In order to differentiate between full and subpixel on each target, truth maps of each target must be created. The truth maps used in this experiment were developed using high resolution visual imagery. Ground truth target spectra were also used to make the comparison for the purpose of classifying a pixel as full, subpixel, shadow, guard, or background. After this classification was completed, a region of guard pixels was labeled around the target. The guard pixel region should not contain any target pixels but the possibility still exists. Adjacency effects and human error in creating the truth maps represent just two factors that make classification of guard pixel necessary. Guard pixels are not counted as detects or false alarms in target detection analysis. In addition, due to the large number of man made targets present in the images, targets other than the designated one are treated as guard pixels and therefore excluded from classification as false alarms or detects.

The calculation of covariance matrices was performed over multiple regions in the scene. Due to the normal distribution assumption in statistical model algorithms, covariance matrices should be calculated over normally distributed data region. Calculating the covariance matrix over the entire image violates this assumption due to the non-gaussian nature of most real scenes.[4, 8] Detection performance is lowered as a result. The inclusion of target pixels in the region over which the background covariance is calculated also negatively impacts detection performance. Three background regions were chosen for this experiment consisting of a tree, grass, and a road region as seen in Figure 5. The tree and grass regions are homogeneous in each run while the road region contains road pixels as well as dirt and grass pixels that line the road. The covariance matrices calculated over these regions for each image were used as the background covariance matrix in each detection algorithm.

Detection results were computed for combinations of target, algorithm, background, and image. A summary of the calculations performed can be seen in Table 1. A road background covariance matrix was not computed or used for the 20000 ft altitude image due to difficulties extracting a statistically large enough road section for covariance calculation. These calculations were performed on each of the the four targets selected.

5. RESULTS

The detection results from each algorithm performed on each image, as described in Table 1, yield a large amount of data. Performing all of these calculations on four seperate targets further increases the result set. Initial analysis has therefore been made using quantitative performance metrics described previously in Section 3.

Detection Rate at False Alarm Rate = 10^{-3}													
Algorithm	Run 5				Run 7				Run 9				
(background)	C5	C6	V	VF	C5	C6	V	VF	C5	C6	V	VF	Average
SAM	.557	.270	.324	.384	.526	.335	.323	.518	.681	.328	.587	.571	.462
ACE (Grass)	.973	.924	.691	.767	.993	.920	.912	.776	1.00	.953	1.00	.034	.679
ACE (Tree)	.937	.897	.686	.540	1.00	.964	.922	.758	1.00	1.00	1.00	1.00	.883
ACE (Road)	.990	.988	.734	.583	1.00	.920	.943	.601					.845
CEM (Grass)	.946	.745	.540	.004	.909	.738	.697	.003	1.00	.857	.955	.028	.619
CEM (Tree)	.748	.401	.372	.001	.775	.722	.524	.007	.894	.724	.681	.006	.488
CEM (Road)	.961	.866	.713	.026	.948	.784	.837	.008					.643

Table 2. Summary of results: Detection rate at a False Alarm rate = .001 (Computed from ROC curves)

ADR													
Algorithm	Run 5				Run 7				Run 9				
(background)	C5	C6	V	VF	C5	C6	V	VF	C5	C6	V	VF	Average
SAM	.858	.771	.792	.983	.841	.777	.874	.996	.929	.884	.952	.983	.887
ACE (Grass)	.994	.992	.915	.990	1.00	.999	.998	.997	1.00	.974	1.00	.989	.987
ACE (Tree)	.987	.960	.769	.807	1.00	.999	.990	.982	1.00	1.00	1.00	1.00	.958
ACE (Road)	.999	.999	.855	.952	1.00	.999	.997	.993					.974
CEM (Grass)	.995	.989	.797	.968	.998	.997	.995	.979	1.00	.990	1.00	.990	.975
CEM (Tree)	.991	.965	.875	.849	.997	.995	.987	.965	.999	.996	.995	.966	.965
CEM (Road)	.999	.997	.896	.970	1.00	.999	.996	.983					.980

Table 3. Summary of results: ADR (Computed from ROC curves)

The results summarized in Table 2 display the DR at a FAR of 10^{-3} as calculated from ROC curves generated from the detection results and truth maps. The average value for each algorithm across all target and image combinations is provided in the last column for overall comparison purposes. It can initially be seen that all other algorithms perform better then the SAM algorithm as would be expected. SAM was included in this comparison to highlight better performance of matched filters. The average results from this metric are highest for the ACE algorithm with various backgrounds and peak when the ACE algorithm is used with a tree background.

Results from another quantitative performance metric, ADR , are summarized in Table 3. This metric and its compliment, AFAR, are both calculated from ROC curves. Only the results for the ADR metric are presented here due to the complimentary nature of these two metrics. Average values for ADR are computed for each algorithm over the range of runs and targets. The range of results using this metric is much smaller than the previous one. A relatively large difference still exists between the SAM algorithm and the others. Comparing results for the ACE and CEM algorithms yields no obvious advantage. The average of all values for ACE and CEM are to close to make a distinction between the two.

These quantitative metrics do not provide a clear picture as to the success or failures in each of these situations. This problem can not be accurately described with a single quantitative value. Visual metrics are necessary to further enhance the algorithm performance in each situation. Raw detection values can be displayed in an image format as in Figures 6(a), 6(b), and 6(c). In these displays, bright values correspond to likely target pixels and guard pixels have been set to black. The ROC curves for these three cases are displayed in Figure 7 along with the ROC curves using three more algorithms. These curves were created using the background pixels from the entire image, not just from the background section used to calculate the covariance matrix. They therefore represent the performance of the algorithm on the entire image rather than on just the selected background section.

From the images in Figure 6(a), 6(b), and 6(c) and the ROC curves in Figure 7 several conclusions can be drawn. The tree background image contains the brightest background pixels and also has the lowest ROC curve using both algorithms. Therefore it can be concluded from these metrics that the tree background provides the
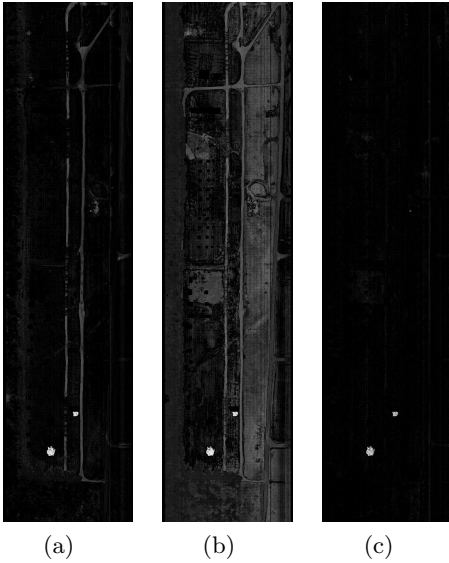
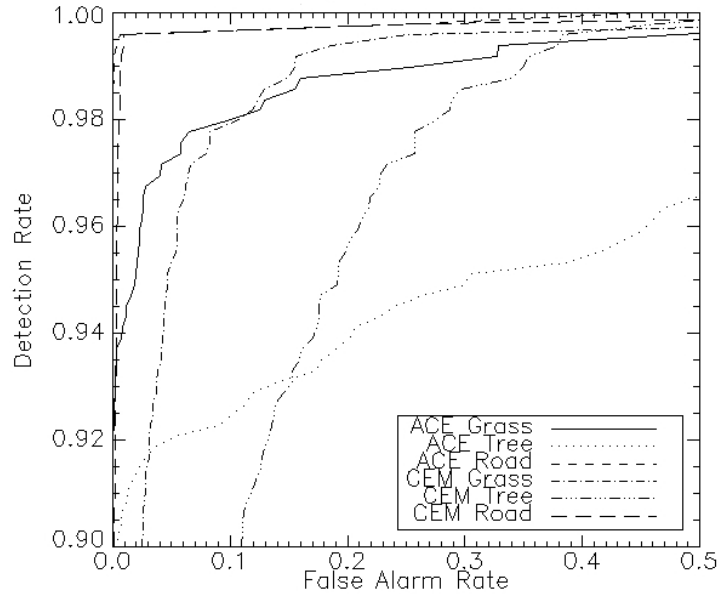**Figure 6.** Results from ACE algorithm using varying backgrounds (a) Grass, (b) Tree, and (c) Road.

Figure 7. Zoom of ROC curves for target C6 using ACE and CEM algorithms.

worst detection results. The road background has the highest ROC curve and the darkest background image. Both of these metrics indicate that the road background results in the highest performance for the image and target combination of Run 5 and target C6 for both the ACE and CEM algorithms. The reason for the success using the road background could be attributed to the fact that road and other man made pixels represent the most likely false alarm pixels in the image.

Further analysis focuses on the ACE algorithm used with grass and tree backgrounds only because road background information was not collected for run 9. The ACE algorithm was chosen due to its success in past literature and the small edge in performance apparent in Table 2.

The final two visual comparison metrics discussed in Section 3 are used to explain the fact that detection performance improves for higher altitude imagery. This fact can be seen in Tables 2 and 3 for nearly all situations. This seems counterintuitive to initial assumptions about the results. One might expect target detection performance to decrease as spatial information decreases. However, it appears that for hyperspectral algorithms, the opposite occurs. In order to understand this situation, the type of target pixel is analyzed further. Specifically, the detection results for full and subpixel targets are seperated and examined independently. Figures 8, 9, 10, and 11 display how the range of detection results vary for background pixels and full and sub pixel target pixels as altitude increases.

The figures for target C5 show a clear trend in the range of results for subpixel targets. The range of values for subpixel targets gets smaller as the altitude of the imagery increases. A similar trend can be seen for full pixel targets in Figure 9. This trend continues when examining the results from target C6 using the ACE algorithm with a tree background (Figure 11) but the opposite phenomenon is seen for the ACE algorithm with a grass background (Figure 10). Full pixel targets once again follow this trend of decreasing in range as altitude increases in Figure 11 but not for Figure 10.

The last visual metric is used to re-examine the previous situations for instances where the results did not follow the described trends. Figure 12 clearly shows the trend described above for subpixel targets but not for full pixel targets. It can be seen in Figure 12(c) that one full pixel target with a detection result around 0.55 alters this trend. The overall range decreases with the exception of this one outlier. The results in Figure 13 deviate from the trend in both target cases. The main two reasons for this deviation are the full and subpixel
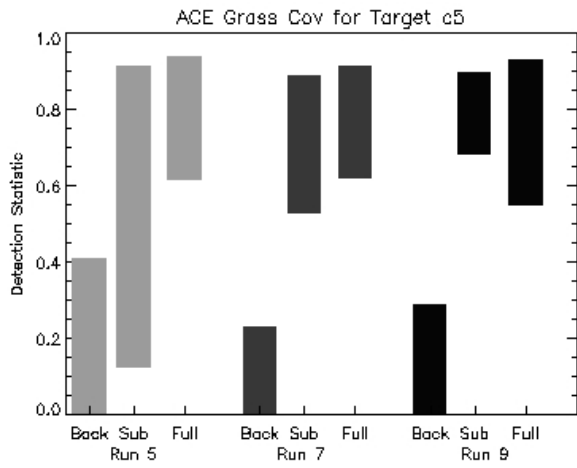
Figure 8. ACE with tree background detection results for target c5: range of values for background, full, and subpixels.
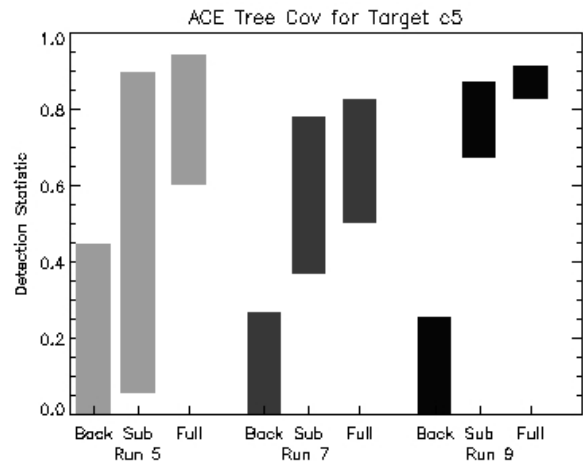

Figure 9. ACE with grass background detection results for target c5: range of values for background, full, and subpixels.
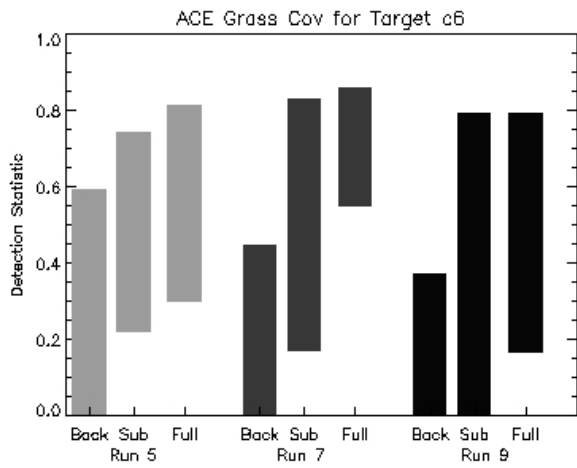

Figure 10. ACE with tree background detection results for target c6: range of values for background, full, and subpixels.
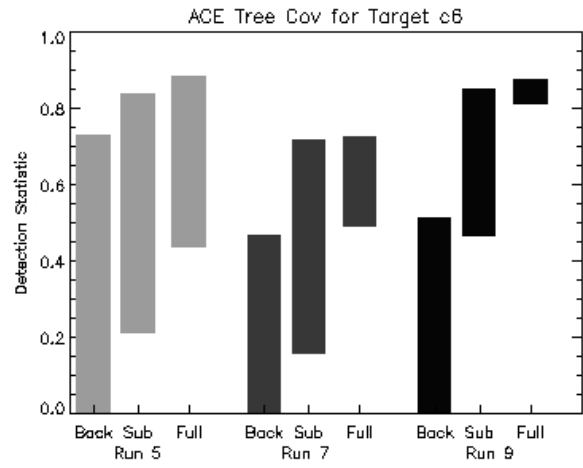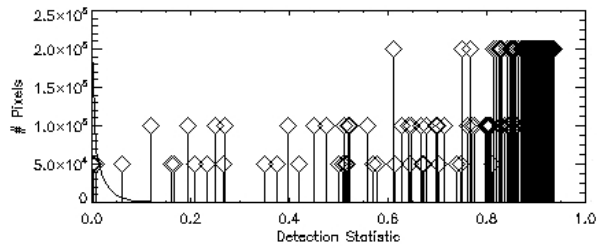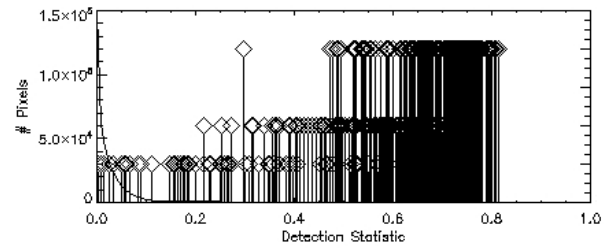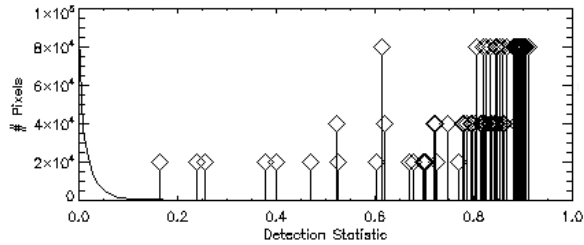

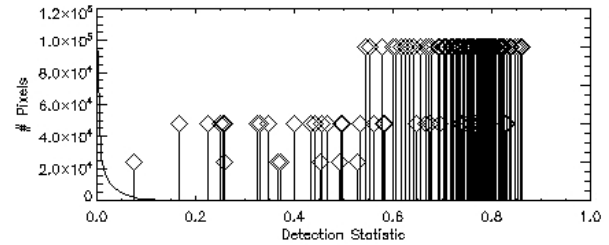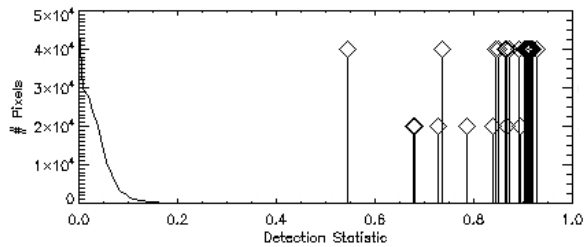**Figure 11.** ACE with grass background detection results for target c6: range of values for background, full, and subpixels.

Figure 12. ACE with grass background displayed as background histogram and target delta functions for target C5 for (a) run 5, (b) run 7, and (c) run 9.

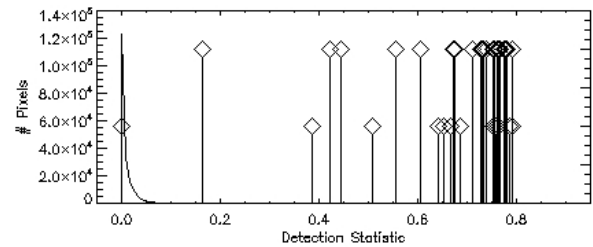**Figure 13.** ACE with grass background displayed as background histogram and target delta functions for target C6 for (a) run 5, (b) run 7, and (c) run 9.

outliers in the results from Run 9. If these two outliers are excluded, the overall background target seperation increases as altitude increases. This would be consistent with previous observations.

A possible explanation for this has to do with the spatial variability of the targets examined. The targets examined were both man-made targets whose library reflectance vector was calculated by averaging multiple measurements of the target over various sections. As the spatial resolution of the imagery decreased, the target pixels were each averaged over a region with more variability in it. Therefore, target pixels at lower spatial resolution more closely resembled the library target reflectance vector used.

6. CONCLUSIONS

This work analyzes target detection results from three algorithms under multiple image, target, and background characteristics. Attempts were made using multiple quantitative comparison metrics to differentiate between the performances of each algorithm. Computing detection rates at a specific false alarm rate yielded a greater range of data and more seperation between algorithms. The ACE algorithm performed best using this metric.

Other comparison metrics were used to describe and analyze the observed trends over increasing altitude imagery. In general, the trend showed that the range of detection results for full and subpixel targets decreased

as the altitude of the image increased. A reason for this phenomenon may be that target pixels imaged at a lower spatial resolution are more similar to the library reflectance vector used. Target information is averaged over a larger region at lower spatial resolutions and more closely resembles the way the target vector was collected.

Further work in this area can extend the size of the data set by including more altitude varying imagery, different targets, and structured as well as unstructured matched filter algorithms.

REFERENCES

1. G. Healey and D. Slater, "Models and methods for automated material identification in hyperspectral imagery acquired under unknown illumination and atmospheric conditions," *IEEE Transactions on Geoscience and Remote Sensing* **37**, pp. 2706-2717, November 1999.
2. D. Manolakis and G. Shaw, "Detection algorithms for hyperspectral imaging applications," *IEEE Signal Processing Magazine* **19**, pp. 29-43, January 2002.
3. D. Manolakis and C. Siracusa and D. Marden and G. Shaw, "Hyperspectral adaptive matched filter detectors: Practical performance comparison," in *Algorithms for Multispectral, Hyperspectral, and Ultraspectral Imagery VII, Proceedings of the SPIE* **4381**, pp. 18-33, 2001.
4. D. Manolakis, "Overview of algorithms for hyperspectral target detection: Theory and practice," in *Algorithms and Technologies for Multispectral, Hyperspectral, and Ultraspectral Imagery VIII, Proceedings of the SPIE* **4725**, pp. 202-215, 2002.
5. L. L. Scharf and L. T. McWhorter, "Adaptive matched subspace detectors and adaptive coherence estimators," *Proc. 30th Asilomar Conference on Signals and Systems*, pp. 1114-1117, 1996.
6. W. H. Farrand and J. C. Harsanyi, "Mapping the distribution of mine tailing in the coeur d'alene river valley, idaho, through the use of a constrained energy minimization technique," *Remote Sensing of the Environment* **59**, pp. 64-76, 1997.
7. P. Bajorski and E. Ientilucci and J. Schott, "Comparison of basis-vector selection methods for target and background subspaces as applied to subpixel target detection," in *Algorithms for Multispectral, Hyperspectral, and Ultraspectral Imagery X, Proceedings of the SPIE* **5425**, pp. 97-108, 2004.
8. D. Manolakis and G. Shaw and N. Keshava, "Comparative analysis of hyperspectral adaptive matched filter detectors," in *Algorithms for Multispectral, Hyperspectral, and Ultraspectral Imagery VI, Proceedings of the SPIE* **4049**, pp. 2-17, 2000.